Journal of Physics B: Atomic, Molecular and Optical Physics

PAPER

Suppression of thermal nanoplasma emission in clusters strongly ionized by hard x-rays

To cite this article: Yoshiaki Kumagai *et al* 2021 *J. Phys. B: At. Mol. Opt. Phys.* **54** 044001

View the article online for updates and enhancements.

IOP ebooks™

Bringing together innovative digital publishing with leading authors from the global scientific community.

Start exploring the collection–download the first chapter of every title for free.

This content was downloaded from IP address 131.169.254.108 on 10/03/2021 at 10:55

IOP Publishing Journal of Physics B: Atomic, Molecular and Optical Physics
J. Phys. B: At. Mol. Opt. Phys. **54** (2021) 044001 (16pp) https://doi.org/10.1088/1361-6455/abd878

Suppression of thermal nanoplasma emission in clusters strongly ionized by hard x-rays

Yoshiaki Kumagai[1,2,*], Zoltan Jurek[3,4,*], Weiqing Xu[1,5], Vikrant Saxena[3,6], Hironobu Fukuzawa[1,7], Koji Motomura[1], Denys Iablonskyi[1], Kiyonobu Nagaya[7,8], Shin-ichi Wada[7,9], Yuta Ito[1], Tsukasa Takanashi[1], Shuhei Yamada[1], Yuta Sakakibara[1], Toshiyuki Nishiyama Hiraki[8], Takayuki Umemoto[9], Minna Patanen[10,11], John D Bozek[10], Ioan Dancus[12], Mihail Cernaianu[12], Catalin Miron[13], Tobias Bauer[14], Melanie Mucke[15], Edwin Kukk[16], Shigeki Owada[7], Tadashi Togashi[17], Kensuke Tono[17], Makina Yabashi[7], Sang-Kil Son[3,4], Beata Ziaja[3,18], Robin Santra[3,4,19] and Kiyoshi Ueda[1,7]

[1] Institute of Multidisciplinary Research for Advanced Materials, Tohoku University, Sendai 980-8577, Japan
[2] Department of Applied Physics, Tokyo University of Agriculture and Technology, Koganei-shi, Tokyo 184-8588, Japan
[3] Center for Free-Electron Laser Science, Deutsches Elektronen-Synchrotron, Hamburg, Germany
[4] The Hamburg Centre for Ultrafast Imaging, 22761 Hamburg, Germany
[5] School of Physical Science and Technology, Shanghai Tech University, Shanghai 201210, People's Republic of China
[6] Department of Physics, Indian Institute of Technology Delhi, New Delhi 110016, India
[7] RIKEN SPring-8 Center, Sayo, Hyogo 679-5148, Japan
[8] Department of Physics, Kyoto University, Kyoto 606-8502, Japan
[9] Graduate School of Advanced Science and Engineering, Hiroshima University, Higashi-Hiroshima 739-8526, Japan
[10] Synchrotron SOLEIL, L'Orme des Merisiers, Saint-Aubin, BP 48, FR-91192 Gif-sur-Yvette Cedex, France
[11] Nano and Molecular Systems Research Unit, Faculty of Science, University of Oulu, P.O.Box 3000, 90014 Oulu, Finland
[12] Extreme Light Infrastructure-Nuclear Physics (ELI-NP), 'Horia Hulubei' National Institute for physics and Nuclear Engineering, 30 Reactorului Street, RO-077125 Magurele, IIfov, Romania
[13] Université Paris-Saclay, CEA, CNRS, LIDYL, 91191, Gif-sur-Yvette, France
[14] Institut für Kernphysik, Universität Frankfurt, Max-von-Laue-Str. 1, D-60438 Frankfurt am Main, Germany
[15] Department of Physics and Astronomy, Uppsala University, P.O. Box 516, SE-751 20 Uppsala, Sweden
[16] Department of Physics and Astronomy, University of Turku, 20014 Turku, Finland
[17] Japan Synchrotron Radiation Research Institute (JASRI), Sayo, Hyogo 679-5198, Japan
[18] Institute of Nuclear Physics, PAS, Radzikowskiego 152, 31-342, Krakow, Poland
[19] Department of Physics, Universität Hamburg, 20355 Hamburg, Germany

E-mail: kumagai@go.tuat.ac.jp and zoltan.jurek@desy.de

Received 20 September 2020, revised 8 December 2020
Accepted for publication 5 January 2021
Published 1 March 2021

Abstract

Using electron and ion spectroscopy, we studied the electron and nuclear dynamics in ~50 000-atom large krypton clusters, following excitation with an intense hard x-ray pulse.

* Author to whom any correspondence should be addressed.

 © 2021 IOP Publishing Ltd Printed in the UK

Beyond the single pulse experiment, we also present the results of a time-resolved, x-ray pump–near-infrared probe measurement that allows one to learn about the time evolution of the system. After core ionization of the atoms by x-ray photons, trapped Auger and secondary electrons form a nanoplasma in which the krypton ions are embedded, according to the already published scenario. While the ion data show expected features, the electron emission spectra miss the expected pump–probe delay-dependent enhancement except for a slight enhancement in the energy range below 2 eV. Theoretical simulations help to reveal that, due to the deep trapping potential of the ions during the long time expansion accompanied by electron–ion recombination, thermal emission from the transient nanoplasma becomes quenched.

Keywords: atomic clusters, x-ray lasers, molecular dynamic, pump–probe spectroscopy, electron and ion spectroscopy, nanoplasma

(Some figures may appear in colour only in the online journal)

1. Introduction

The advent of x-ray free-electron lasers (XFELs) [1–3], namely the free electron laser in Hamburg (FLASH) which began operation in 2005, followed by the Linac Coherent Light Source (LCLS, 2009) in the USA and the SPring-8 Angstrom Compact free electron LAser (SACLA, 2011) in Japan, has opened new avenues to a wide spectrum of research fields, e.g. the discovery of nonlinear processes driven by intense x-ray fields [4–6], the observation of ultrafast transitions in optically dressed matter [7–9], and the determination of unknown structures of nanometer-size samples [10–12]. In recent years, new XFEL facilities have begun operation [13–15], promising to develop further the science and technology of XFELs. To achieve these ambitious goals, the understanding of the intense x-ray pulse–matter interaction and the subsequent processes is essential for developing applications using XFELs [16, 17].

To investigate light-induced dynamics, atomic clusters are ideal objects because their size can be varied in a controlled way from a single atom to a bulk-like macroscopic object [18, 19]. In the case of a nanometer-sized bonded atomic assembly irradiated by a single intense x-ray pulse, hot nanoplasmas can be formed due to the energy absorption from the electromagnetic field [20–22].

In extreme ultraviolet (XUV) fields, nanoplasma formation is driven by sequential single-photon ionization of valence electrons of the atoms [23, 24]. Because of their low kinetic energies, almost all electrons ejected in photoabsorption events participate in forming the plasma. In this photon energy regime [25, 26], the disintegration of excited clusters is driven by Coulomb explosion [27] and hydrodynamic expansion [28, 29]. Electron–ion recombination processes, which become significant on long cluster expansion timescales, play a crucial role in creating the final ionic charge states of the cluster fragments. As a result, the number of ions with higher charge states is reduced compared to the instant just after the ionizing light pulse [30]. Recent studies in this regime [31–33] have reported that a large number of Rydberg atoms are formed during the first few picoseconds of the cluster expansion, due to electron–ion recombination.

In contrast to the XUV case, nanoplasma formation by x-ray pulses, with sufficient photon energy to ionize atomic inner-shells, is a rather indirect process at currently achievable photon fluxes [22]. In light elements, an inner-core hole state is created in a photoabsorption event. This is then followed by an Auger decay, giving rise to the emission of Auger electrons. The energetic photo- and Auger electrons can excite more electrons within the cluster through sequential electron impact ionization (also called collisional ionization), which proceeds until the impact energies of the electrons are so low that no further ionization is possible. The most energetic electrons escape from the system and leave behind a highly charged cluster (see, e.g., a detailed study for neon in [34]).

In a cluster composed of heavy atomic species, the hard x-ray-induced nanoplasma formation is even more complex because deep inner-shell ionization of heavy atoms is followed by a cascade of Auger decays producing many Auger electrons at various energies. These electrons can excite further electrons within the cluster through sequential electron impact ionization. The low-energy electrons, produced via low-energy Auger electrons that lost their energy via inelastic scattering and also via electron impact ionization, are then trapped by the cluster potential, forming a nanoplasma. Such indirect ionization processes are specific to the heavy elements irradiated by hard x-ray photons.

Here, we report on experimental studies of nanoplasma formation in large krypton clusters ($\langle N \rangle \sim$ 50 000) irradiated by hard x-ray pulses from the free-electron laser SACLA [3]. We studied the disintegration of the clusters by laser pulses of 14.5 keV and 5.6 keV photons which create different core holes in krypton atoms, namely, K- and L-shell holes, respectively. The ion data recorded after the impact of 14.5 and 5.6 keV photons show very similar trends. To extend the insight, we applied another pulse created by a near-infrared (NIR) laser to probe the nanoplasma formation dynamics in time, similarly to our previous study [35]. The

Table 1. XFEL parameters employed in the experiment.

Photon energy	keV	5.6	14.5
Photon band width	eV (FWHM)	110[a]	130[a]
Focal beam size (horizontal)	μm (FWHM)	$\sim$1.1[a]	$\sim$1.0[a]
Focal beam size (vertical)	μm (FWHM)	$\sim$1.0[a]	$\sim$0.9[a]
Repetition rate	Hz	30	
Pulse duration	fs (FWHM)	$<$ 10[b]	
Average pulse energy	μJ/pulse	18[c]	40[c]
Pulse energy fluctuation	%	$\pm$10[a]	$\pm$11[a]
Peak fluence[e]	μJ/μm^2	$\sim$15[d]	$\sim$39[d]
Peak photon fluence	Photons/μm^2	$\sim 1.7 \times 10^{10}$	$\sim 1.7 \times 10^{10}$

[a]Measured.
[b]Estimated [39].
[c]Calculated from the measured pulse energy by considering the transmittance of the beamline, beryllium windows and Kirkpatrick–Baez mirrors.
[d]Calculated from the average pulse energy and the focal beam size [40].
[e]Pulse-averaged peak fluence in the center of the focus.

electron spectra show exponential-like features in the energy regime up to 150 eV, typically interpreted as signatures of thermal nanoplasma emission (e.g. [22, 36]); here, surprisingly, the exponential-like features lack any delay dependence. This is unexpected as it is well known that at resonance conditions a nanoplasma can be heated efficiently by an NIR pulse, resulting in increasing temperature, shown by pump–probe delay-dependent electron yields.

In order to theoretically examine the dynamics of such XFEL-ionized clusters, we employed our molecular-dynamics simulation tool XMDYN [37, 38] (also used in previous studies [35, 36]). We tracked the early-stage ($<$1 ps) electron and nuclear dynamics for krypton clusters consisting of $\sim$1000 up to $\sim$50 000 atoms (the latter coinciding with the target size in the experiment) after irradiation with 5.6 keV photons. The simulation revealed a slow expansion and a deep trapping potential in larger clusters. The generated potential well can capture quasi-free electrons in the nanoplasma over such long times that the electron nanoplasma vanishes due to recombination and correlated emission processes before a detectable thermal emission feature can develop in the spectra. The numerical results also indicated that the exponential-like feature of the experimental electron spectrum in the regime up to 120 eV is formed by electrons produced, within a few tens of femtoseconds in the early stage of the x-ray-induced dynamics, via collisional ionization triggered by photo- and Auger electrons.

In the present report we also discuss experimental evidence that Rydberg atoms are efficiently produced as a consequence of the electron–ion recombination during the slow nanoplasma expansion.

2. Experiment

The measurements were carried out at experimental hutch EH4 of beamline BL3 [40] of the XFEL facility SACLA [3], in Japan. Details of the experimental apparatus are described elsewhere [35]. We used x-ray pulses at two photon energies, 5.6 and 14.5 keV, which were above the binding energies of the L- and K-shell levels for krypton atoms, respectively. Table 1 shows all relevant parameters of the XFEL beam at each photon energy. The XFEL beam was focused on the interaction point by a Kirkpatrick–Baez mirror arrangement [41]. The pulse duration was estimated to be $<$10 fs [39]. The pulse energies were measured shot-by-shot by the beam-position monitor [42] located upstream of the beamline and calibrated by a calorimeter. The ratio between the pulse energies for the two photon energies was set in such a way that the respective photon fluence values were approximately equal to each other. The relative intensity per XFEL pulse was measured using a p–intrinsic–n photodiode located downstream of the interaction point. The peak fluence at 5.6 keV photon energy was calibrated, using the charge distribution of highly charged ions from isolated argon atoms [43, 44]. We note that the calibration method [43, 44] may overestimate the peak fluence by a factor of up to two in the moderate-fluence regime (i.e. where the multiple photoabsorption in the isolated argon atoms is weak) [35].

The clusters were prepared by adiabatic expansion of krypton gas through a nozzle with 300 μm diameter and 15° half-opening angle at 300 K. The stagnation pressure was 1.2 MPa, and the average cluster size was estimated to be $\langle N \rangle \sim 50\,000$ atoms, according to a well-known scaling law [45]. The radius of the Kr_{50000} cluster was 82 Å. The cluster beam was collimated by two skimmers at 20 and 400 mm from the nozzle. The inner diameters of the first and second skimmers were 0.5 and 2 mm, respectively. The distance between the second skimmer and the interaction point was 250 mm. The cluster beam was perpendicular to the propagation direction of the x-ray beam. Its transverse size at the reaction point was estimated to be $\sim$2 mm (FWHM), i.e. shorter than the Rayleigh lengths of $\sim$11 mm (5.6 keV) and $\sim$24 mm (14.5 keV). Thus, the electron and ion source volume had a cylindrical shape of $\sim$1 μm in diameter and $\sim$2 mm along the XFEL beam.

An NIR laser with a wavelength of 800 nm was used to probe the expansion of XFEL-ionized clusters. The NIR laser with a focal size of 120 μm (FWHM) overlapped with the XFEL beam focus with a small crossing angle (less than 1°) at the interaction point. The pulse duration of the NIR laser was 54 fs (FWHM) and the intensity was 5.0×10^{13} W/cm^2. In separate measurements (not shown), in which we irradiated the krypton clusters using only NIR laser pulses, we verified

that at this intensity the NIR-induced nanoplasma formation was negligible.

The intrinsic temporal resolution in such pump–probe experiments, determined by the temporal durations of the XFEL and NIR pulses, is significantly limited by a temporal jitter between the two pulses [46]. In the present experiments, the arrival times of the XFEL and NIR laser pulses were not monitored; thus, the temporal resolution of the pump–probe delays was estimated to be ∼800 fs (FWHM), corresponding to the typical temporal jitter between the XFEL and NIR pulses [47]. More details on the pump–probe scheme are described elsewhere [35].

An electron velocity-map-imaging spectrometer [22, 36, 48] and an ion time-of-flight (TOF) spectrometer [36, 48] recorded the kinetic-energy spectrum of electrons and ionic fragments as a function of the time delay between the XFEL-pump and NIR-probe pulses. The mass (m) resolution of the TOF spectrometer for nonenergetic ions, defined as $m/\Delta m$, was typically ∼450.

3. Numerical simulations

In order to theoretically describe the electron and nuclear dynamics of the XFEL-ionized clusters, we employed the simulation tool XMDYN [37, 38]. The code uses the classical molecular-dynamics technique to track the real-space dynamics of atoms, atomic ions, and emitted electrons. Charged particles interact with each other via soft Coulomb interaction according to the $1/\sqrt{r^2 + r_0^2}$ distance dependence. The non-zero r_0 parameter removes the singularity for zero interparticle distance, $r = 0$, in order to stabilize the numerical propagation. Atomic bound electrons are described (up to the 4p orbital) via the orbital occupation numbers of the individual atoms (*quantum-modeled* electrons). Ionization events, at which the emitted electrons appear as *classical* particles and the occupation numbers of the involved atomic orbitals change, are handled within a Monte Carlo scheme. The framework treats photoionization, Auger and fluorescent decays, collisional ionization, and recombination. For these processes the implementations described in detail in reference [38] were used. Within the simulation framework the recombination is modeled classically, i.e. while evaluating saved snapshots at post-processing of the simulation results, classically trapped electrons are identified and the bare ionic charges are modified accordingly. We chose $r_0 = 1.1$ Å so that electrons classically captured in the bottom of ionic potentials had binding energies that reasonably compared with the real ionization energies of the ground-state Kr ions, i.e. the model/real ionization energies are: 11.9 eV/13.0 eV, 23.8 eV/23.9 eV, 35.7 eV/35.8 eV, 47.6 eV/48.5 eV, 59.5 eV/62.0 eV, 71.4 eV/76.3 eV, 83.3 eV/91.2 eV, 95.2 eV/111 eV, 107 eV/132 eV, and 120 eV/154 eV for Kr charge states 0, +1, +2,…, and +9, respectively. A similar strategy was used in reference [26]. In previous works [35, 36], we introduced extensions of the code to capture phenomena needed in order to study oligomer formation within weakly ionized clusters, namely: van der Waals interaction, chemical bond formation and charge transfer. However, as these new algorithms are computationally demanding, currently, it is not feasible to propagate a 50 000-atom cluster up to picosecond times with a full simulation. Therefore, we switched the three new capabilities off. In this way, we sacrificed the possibility of forming oligomers in the simulation, but we were still able to capture with a reasonable accuracy the electron dynamics that were shown not to be sensitive to the chemical details [36].

Various complex decay channels appear in a cluster environment due to interatomic or atomic electron–plasma electron correlations, such as interatomic Coulombic decay (ICD) [49], electron-transfer-mediated decay (ETMD) [50], collective autoionization [51] and correlated electronic decay (CED) [52]. Using long wavelength excitation, it has been shown that in many-atom (e.g. cluster) systems these phenomena may contribute significantly to the relaxation processes and energy release. In the case of hard-x-ray excitation, the radiation creates primarily core holes in the electronic structure. Core holes decay on the sub-femtosecond timescale (except for 3d holes, which decay within ∼8 fs) due to strong intra-atomic electron correlations, faster than even the shortest, ten-femtosecond-timescale interatomic decay processes take place. These correlated processes are the Auger decays traced by our simulations. Further, the molecular-dynamics treatment of activated (ionized) electrons automatically opens the possibility for correlated (e.g. ICD-like, autoionization or CED) processes involving high-lying Rydberg states, similarly to the classical treatment in reference [52, 53]. However, we also note that correlated processes that involve both *classically treated* electrons and *quantum-modeled* states (e.g. Auger processes or ICD, when both *quantum-modeled* valence state(s) and *classical* Rydberg electron(s) are involved) and processes in which *quantum-modeled* states of different atoms participate (e.g. ETMD or a subset of ICD processes) are not yet included in our model.

4. Results and discussion

4.1. Electron emission in atomic processes

In this section, we provide an overview of those atomic ionization processes that play a predominant role in shaping the cluster dynamics. In krypton, under the experimental irradiation conditions, the ejected electrons can be grouped into two distinct sets based on their initial kinetic energy. We refer to electrons with initial energy from a few eV up to a few hundred eV as *slow* electrons. The other group of electrons comprises those with initial kinetic energy above 1.2 keV, referred to as *fast* electrons.

At 5.6 keV photon energy, the L-shell is the deepest shell available for photoionization, which defines at the same time the most probable photoionization channel. Under the irradiation conditions used in the experiment, approximately 5% of the atoms in the focus of the XFEL beam absorb a photon (the cross section for L-shell photoionization is 0.03 Mbarn [54]). This means that, although for a single atom the probability for absorbing two or more photons is rather small, a 50 000-atom cluster still absorbs ∼2500 photons. Photoionizations release *fast* photoelectrons from the 2s and 2p orbitals with kinetic

energy of 3.7 keV and 3.9 keV, respectively. In addition, L-hole relaxation via Auger decay leads to the ejection of a *fast* electron. In all other Auger processes, with the involvement of a higher-shell vacancy, *slow* electrons are emitted.

At 14.5 keV, the possibility of K-shell photoionization opens up. Although the photon fluence in this case is approximately the same as in the 5.6 keV case, the probability of core photoionization (K-shell ionization being the predominant channel) drops by ∼50% because of the smaller cross section (0.015 Mbarn [54]). The photon energy is ∼480 eV above the K-edge. Therefore a *slow* photoelectron is released. The K-hole is predominantly filled either by an electron from the L-shell in a fluorescence process (releasing no electron) or in a KLL Auger process releasing a *fast* electron and creating double L-holes at the same time. The branching ratio between the fluorescence and Auger processes is approximately 2:1. Note that after the fluorescence event an L-hole state is created, just like after the L-shell photoionization of a neutral krypton atom.

In a dense atomic environment, collisional ionization is a major source of ionization. In a collisional ionization event, a free electron transfers energy to a bound atomic electron, making the latter capable of leaving its parent atom. In such a process, the released (secondary) electron is typically a *slow* one. The probability of collisional ionization in a medium is often described by the mean free path λ, which depends on the cross section of the process σ and the density of the material n, via the formula $\lambda = (\sigma n)^{-1}$. The mean free path has a minimum of 8 Å at 40 eV electron energy in a neutral krypton cluster and increases monotonically with the increase of the primary electron energy [55]. For example, for 250 eV, 500 eV and 1.2 keV energies, the mean free paths are 20 Å, 30 Å and 60 Å, respectively [55].

4.2. Cluster dynamics triggered by an XFEL pulse: experimental results

The ion TOF spectra from the krypton clusters after the irradiation with 14.5 and 5.6 keV pulses are presented in figures 1(a) and (b), respectively. The peaks of the highly charged atomic ions Kr^{q+} ($q = 2$–10) and singly charged oligomers Kr_n^{1+} ($n = 1$–5) are clearly identified.

The peaks of Kr^{q+} ($q = 3$–10) were narrow enough to resolve isotopes at different charge states, since they were produced only from the unbonded single atoms also present in the beam. At the present peak fluence, the contribution of the sequential multiple-photon absorption by an atom [43] is negligible. Therefore, the extracted charge state distributions (figure 1(c)) correspond to the case of single photoabsorption (see e.g. [56, 57]). The charge states produced by L-shell ionization are distributed up to Kr^{9+}, peaking at Kr^{5+}, with a mean charge state of +5.1. In contrast, for K-shell ionization the charge states are distributed more widely, up to Kr^{12+}, with a mean charge state of +6.0. The data between Kr^{3+} and Kr^{7+}, however, look the same up to a scaling factor of ∼3. This can be traced back to the difference between the core-photoionization cross sections in the two cases and to the branching ratios of the decay channels filling the K-hole (we note again that the photon fluence is approximately the same).

The number of K-holes created at 14.5 keV is smaller by 50% than the number of L-shell holes created at 5.6 keV (because of the difference in cross sections). Of all the K-holes, 66% end up as a single L-hole. The fate of an ion from this point onwards is the same as after an L-shell photoionization event. This leads to a reduction of 50% × 66% = 33%, capturing the factor of ∼3 difference between the middle parts. When Auger decay occurs, double L-holes are formed, opening the possibility to reach significantly higher charge states, thus affecting the yield of the highest charge states (i.e. >7).

In figures 1(a) and (b), the broad peaks of Kr_n^{1+} ($n = 1$–5) ions (e.g., the peak width of Kr^{1+} is ∼180 ns (FWHM)) give evidence that these ions were produced via explosion of highly charged krypton clusters, while the narrow peaks of nonenergetic Kr^{q+} ($q = 3$–10) ions were produced only from isolated atoms. Kr^{2+} ions were produced from the ionization of both clusters and isolated atoms. The fact that no highly charged ions Kr^{q+} ($q > 2$) emitted from the cluster have been observed in the experiment shows that the charge accumulated in the initially core-ionized atoms must have been quickly distributed over the whole cluster before the cluster disintegration took place. In our previous work on argon clusters [36], ionic oligomers were observed, indicating that chemical bonds formed in the ionized rare gas system survive to a large extent during the XFEL irradiation. In figure 1(d), the extracted charge state distributions show a trend similar to that found in reference [36] (note that all experimental signals are volume integrated, i.e., they integrate signals from clusters irrespective of their positions within the focus profile of the beam at the time of irradiation [58]). The most abundant ion is Kr^{1+}. According to the yields, most of the cluster charge is stored in Kr^{1+} ions after disintegration.

While for isolated atoms the ratio between the total ion counts at 5.6 and 14.5 keV (dominated by charge states of +4 up to +7) was ∼3, for clusters (dominated by Kr^{1+}) we found a factor of approximately 2. This factor can be estimated by also considering the Auger electron energies beyond the branching ratios of decay processes. We made this estimation for a cluster of 50 000 atoms at half of the peak fluence, i.e., at 7.8×10^9 photons/μm^2, in the following way.

With 5.6 keV photons, approximately 1250 L-shell photoionization events occur, releasing *fast* photoelectrons, followed by roughly 1250 Auger decays also releasing *fast* electrons. Now we assume that all the *fast* electrons can leave the system and the *slow* ones cannot. Then, the potential on the surface of a spherical cluster with 82 Å radius, possessing a charge of +2500, is 440 eV. This value justifies the initial assumption of trapping *slow* electrons but releasing *fast* ones. This assumption is further backed up by considering that *slow* electrons lose additional energy via collisional ionization. Therefore, we estimate that the cluster acquires a total charge of +2500.

At 14.5 keV, ∼625 K-shell photoionization events occur, ejecting *slow* photoelectrons. Because of the 2:1 branching ratio between the relevant fluorescence and Auger processes, there are 416 L-hole states that will release 416 *fast* electrons via consecutive Auger decays. Further, 208 KLL Auger events release 208 *fast* Auger electrons and create 208 double-L-hole

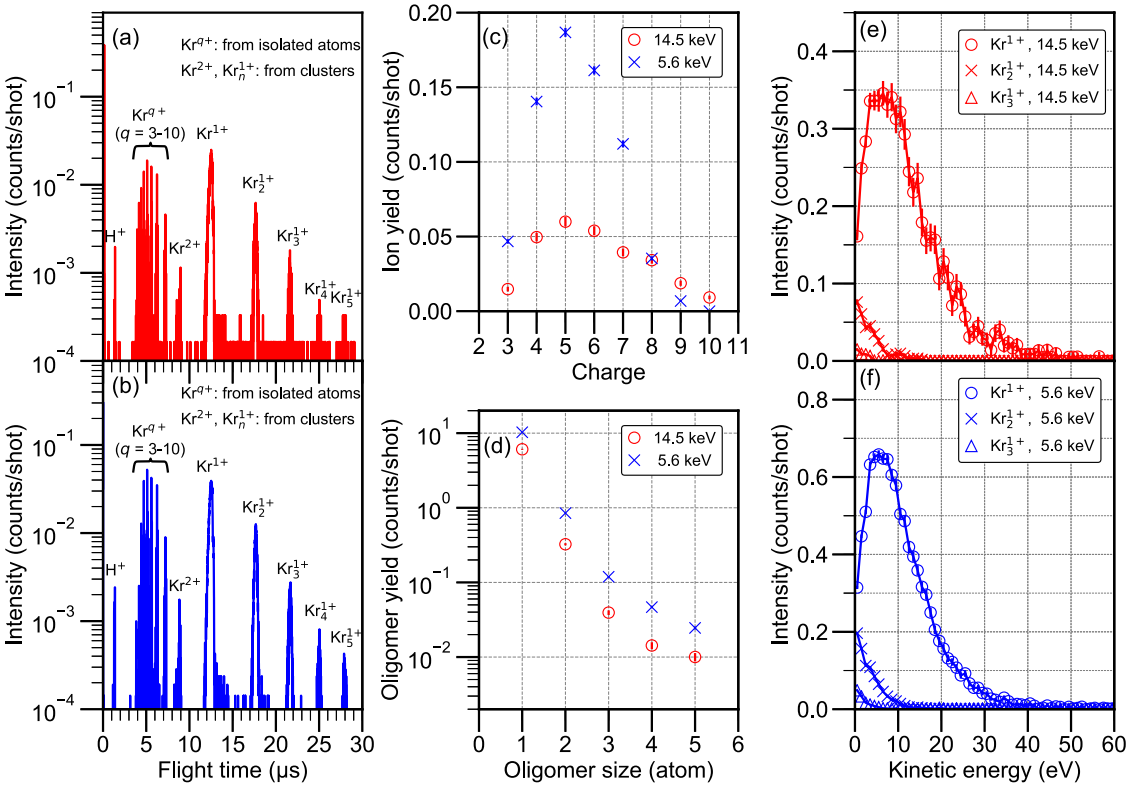

Figure 1. Experimental ion TOF spectrum from Kr_{50000} after excitation with XFEL pulses at a photon energy of (a) 14.5 and (b) 5.6 keV. The peaks correspond to highly charged monomers Kr^{q+} ($q = 2$–10) and singly charged oligomers Kr_n^{1+} ($n = 1$–5). (c) Yield of highly charged ions, recorded at the irradiation of isolated atoms (red: 14.5 keV, blue: 5.6 keV), as a function of charge state $q = 3$–10. (d) Oligomer ion yields, recorded at the irradiation of krypton clusters (red: 14.5 keV, blue: 5.6 keV), as a function of oligomer size. (e) and (f) Kinetic energy spectra (KES) of singly charged oligomer fragments (Kr^{1+}, Kr_2^{1+}, Kr_3^{1+}) after ionizing the clusters with XFEL pulses at a photon energy of 14.5 and 5.6 keV, respectively.

states, where we assume that a double-hole state will simply create 2×208 *fast* Auger electrons. Altogether we end up creating $416 + 208 + 2 \times 208 = 1040$ *fast* electrons. Assuming that all *fast* electrons can escape, the cluster charge reaches $+1040$, which is close to half of the cluster charge at 5.6 keV.

The kinetic energy spectra (KES) of singly charged oligomer fragments, Kr^{1+}, Kr_2^{1+} and Kr_3^{1+}, after ionization of clusters by XFEL irradiation with photon energy of 14.5 keV and 5.6 keV are shown in figures 1(e) and (f), respectively. The oligomers, in particular the singly charged ones, show distributions that are qualitatively independent of the used x-ray photon energy, up to a scaling factor. This finding is a consequence of the fact that the fragmentation of the outer and inner parts is driven mainly by Coulomb explosion and hydrodynamic expansion, respectively, both dynamics exhibiting scalability. In a quasi-neutral nanoplasma produced from clusters of a given size, the kinetic energy distribution of ions mainly depends on the net charge and the quasi-free electron energy [59].

In figure 2, we show electron KES from krypton clusters consisting of ∼50 000 atoms after excitation with XFEL pulses at photon energies of 14.5 keV and 5.6 keV. Let us first focus on the 0–150 eV wide range of the spectrum recorded at 14.5 keV photon energy (figure 2(a)). The electron KES may be divided into two regimes: an unstructured high-energy contribution from ∼20 to 150 eV and a shoulder-like structure below ∼20 eV. One can fit the spectrum by the sum of two exponential decay curves (i.e. the two straight dashed-lines in figure 2(a)), which capture the electron KES up to 150 eV (blue solid curve in figure 2(a)). The green dashed line, which represents the unstructured high-energy contribution from ∼20 to 150 eV, gives an exponential decay with a decay constant of 62 eV, while the yellow dashed line represents the shoulder-like structure below ∼20 eV with an exponential decay constant of 4.7 eV.

At this stage one may be tempted to use both of these slopes as extracted kinetic temperatures of the emitted nanoplasma electrons. However, as discussed in the forthcoming subsections, in our experiment the electrons comprising the 20–150 eV feature do *not* originate from thermal electron evaporation from the nanoplasma.

Figures 2(b) and (c) also show the KES of the electrons at 5.6 keV photon energy. While details of the spectrum in the 1–20 eV range exhibit differences compared to the higher-photon-energy case, the curve runs close to the exponential fit at 14.5 keV, meaning that the general trend agrees well at different photon energies. Unfortunately, there are no experimental data available in the 20–150 eV range at 5.6 keV photon energy. However, as all other electron and ion spectra discussed before show a behavior independent of the photon energy, it is reasonable to also expect an exponential behavior in the 20–150 eV range for the 5.6 keV photon energy.

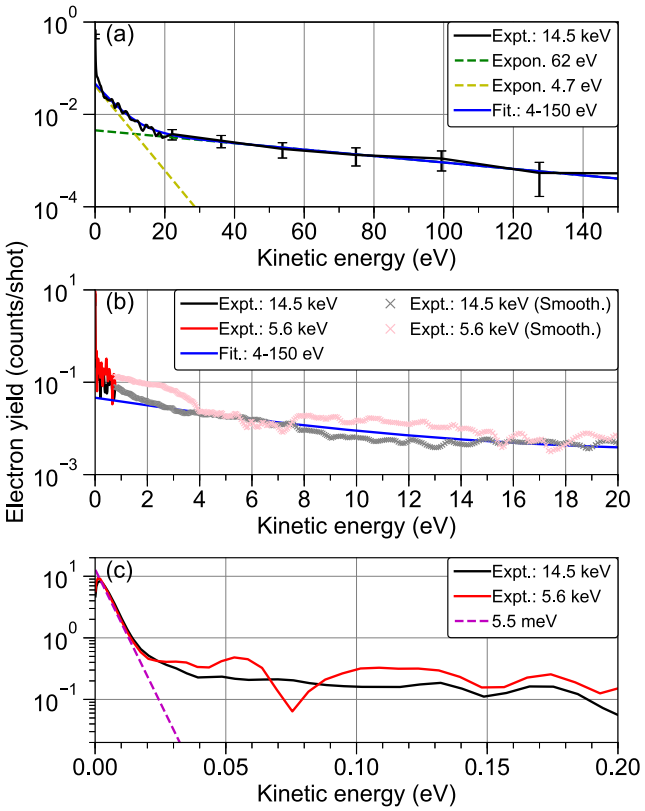

Figure 2. Experimental KES of electrons in the energy range up to (a) 150 eV, (b) 20 eV and (c) 0.2 eV from Kr_{50000} clusters after excitation with x-ray laser pulses. Black and red curves show the experimental spectrum at 14.5 keV and 5.6 keV, respectively. Gray and pink crosses show the experimental results above 0.8 eV smoothed using a moving average. Yellow, green and purple dashed lines represent exponential functions with decay constants of 62 eV, 4.7 eV and 5.5 meV, respectively. The blue solid line is the sum of the yellow and green lines.

Figure 2(c) is a zoom-in of the spectra below 0.2 eV. We can see a dramatic increase in intensity toward zero energy below 0.02 eV. The purple dashed line in figure 2(c) is an exponential function with a decay constant of 5.5 meV. Similarly strong emission of low-energy electrons in the meV range has been observed in velocity-map-imaging experiments with XUV ionization fields, and has been attributed to the efficient DC field re-ionization of high-lying Rydberg states during nanoplasma expansion [31].

4.3. XFEL pump–NIR probe experimental results

To experimentally probe the intermediate state of the XFEL-induced nanoplasma, we used time-resolved electron and ion spectroscopy by applying the x-ray pump–NIR probe method [35]. The ion KES are shown as a function of the time delay between XFEL and NIR pulses in figure 3. The measured ion data show enhancement of the Kr^{1+} and Kr^{2+} ion yields around 1 ps delay. The phenomenon has been reported in earlier studies [35]. The observed enhancement of the ion yields may be attributed to further ionization by the NIR due to the surface plasmon resonance effect [19, 60]: when the resonance condition, depending on the frequency of the NIR laser

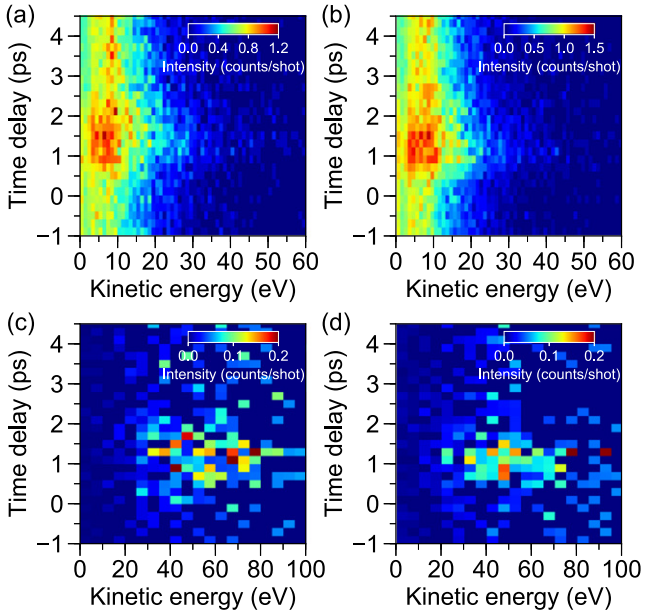

Figure 3. Experimental KES of ions (Kr^{1+} and Kr^{2+}) from Kr_{50000} clusters as a function of XFEL pump–NIR probe time delay; (a) Kr^{1+}, 14.5 keV, (b) Kr^{1+}, 5.6 keV, (c) Kr^{2+}, 14.5 keV, (d) Kr^{2+}, 5.6 keV.

and the electron density, is fulfilled, the quasi-free electrons of the nanoplasma can acquire significant additional kinetic energy from the field and further ionize (in collisional ionization events) neutral Kr atoms and Kr^{1+} ions to Kr^{1+} and Kr^{2+} ions, respectively.

The surface plasmon resonance effect for homogeneous nanoplasmas has been described by Ditmire *et al* [60] in the following way. The heating rate of the cluster due the laser depends on the electron density n_e inside a spherical cluster. When this density is high, i.e. $n_e/n_{crit} \gg 3$ (where the critical electron density is $n_{crit} = m_e\omega^2/4\pi e^2$ with the used laser frequency ω, the electron mass m_e and elementary charge e), then the laser field inside is screened by the charges in the nanoplasma, and is weaker inside the cluster than outside. For instance, this can be the case when the nanoplasma is formed right after the ionizing pulse. Thus, the screening effect hinders heating at short delays. The electron density, however, decreases with time due to nanoplasma expansion [27–29], thermal electron emission [22], and electron–ion recombination within the nanoplasma [20, 31]. As the system evolves on the picosecond timescale, the resonance condition $n_e/n_{crit} = 3$ is met, and the field can penetrate inside and the heating rate in the cluster becomes enhanced. The value of the critical density n_{crit} is 1.7×10^{21} cm^{-3} for an 800 nm NIR laser. Therefore, one can conclude, based on the experimental ion data, that the electron density reaches the value of $3n_{crit} = 5.1 \times 10^{21}$ cm^{-3} at $\sim$1 ps after irradiation.

Though the behavior of the ion yields as a function of delay is similar to the one found in our earlier study [35] (making its interpretation rather straightforward), the electron spectra in the range of 0–20 eV do not show any delay dependence as shown in figures 4(a) and (b), except for the range below $\sim$0.2 eV which exhibits an increase around 1 ps as

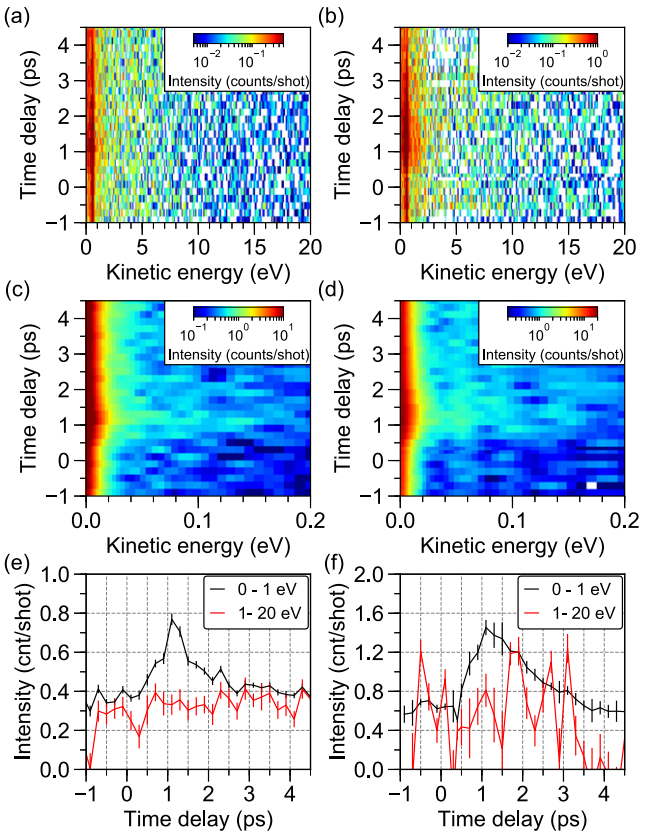

Figure 4. Experimental KES of electrons in the energy range up to 20 and 0.2 eV from Kr_{50000} clusters as a function of XFEL pump–NIR probe time delay; (a) and (c) 14.5 keV, (b) and (d) 5.6 keV. Integrated electron yields over the ranges 0–1 eV and 1–20 eV as a function of time delay at (e) 14.5 keV and (f) 5.6 keV photon energies.

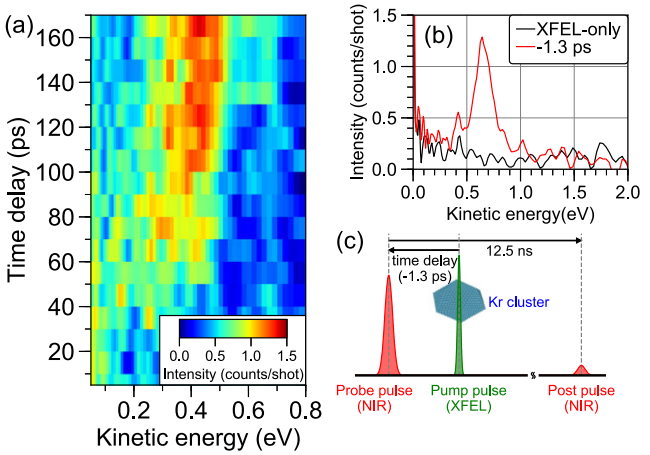

Figure 5. (a) Experimental KES of the electrons from Kr_{50000} clusters as a function of the XFEL pump–NIR probe time delay. The photon energy of the XFEL pulse is 5.6 keV. (b) KES at −1.3 ps time delay (red). The black curve is the KES without applying the NIR pulse (XFEL-only case). (c) Schematic of the temporal configuration for the present XFEL pump–NIR probe setup, also showing the post-NIR pulse.

in zoomed-in figures 4(c) and (d). Figures 4(e) and (f) show integrated yields for the low (0–1 eV) and medium (1–20 eV) energy electrons, as a function of time delay. Enhancement of the yields is apparent only for the low-energy but not for the medium-energy electrons. This finding has several consequences. One is connected to the fact that the experimental signal is volume integrated, i.e. it contains contributions from all fluence regions of the beam focus. If a delay-independent feature comes from clusters in the focus, i.e. exposed to high intensity, it must have developed earlier than ∼1 ps; otherwise, it should have been enhanced once energy was absorbed from the NIR at resonance. Furthermore, any signal that comes from clusters in regions of sufficiently low intensities (i.e. where the critical electron density is never reached due to insufficient ionization) is expected to be independent of the delay. Numerical simulations, discussed in the following subsection, can help to clarify which scenario describes our data.

The other consequence is that the ion yield enhancement is connected to very low-energy electron emission, indicating that these electrons escaped in a very late phase of the expansion. Similar enhancement in low-energy electron emission below a few hundred meV has been reported, using electron spectroscopy with an NIR pump–NIR probe scheme [61].

Finally, we discuss a feature of the electron spectrum that serves as another signature of the presence of highly excited Rydberg atoms. Figure 5(a) shows the time-resolved electron KES at 5.6 keV as a function of the time delay up to 170 ps. An additional photoemission line appears around 50 ps time delay and remains strong for all longer delays, with a slight shift to higher energies and becoming narrower with increasing time delay. This additional photoemission line can be ascribed to the reionization of excited atoms formed by electron–ion recombination (REAR) during the cluster expansion [32]. In a previous work on argon clusters using an XUV pump–NIR probe scheme [32], it was reported that the time evolution of REAR peaks reflects the time evolution of the environment of the re-ionized atoms in the cluster. The cluster potential and the interaction with the neighboring ions induce a kinetic energy downshift that disappears for a long time delay, when the influence of the environment can be neglected.

Figure 5(b) shows the electron KES of krypton clusters with an average size of ∼50 000 atoms irradiated by 5.6 keV XFEL and NIR laser pulses with a time delay of −1.3 ps (meaning that the NIR laser pulse arrives at the reaction point earlier than the XFEL pulse). While in an NIR-only or XFEL-only experiment the REAR feature is completely missing, the peak does exist for negative delays, without any temporal overlap between the two pulses. This finding can be attributed to the existence of post-NIR pulses (see schematic of temporal configuration in figure 5(c)). The repetition rate of the NIR laser was 80 MHz. NIR pulses arriving synchronized with the XFEL pulses (coming at a much lower 30 Hz repetition rate) were amplified by three orders of magnitude. However, other unamplified pulses also hit the interaction volume, the first one arriving $(80\ \text{MHz})^{-1} = 12.5$ ns after the main pulse.

The REAR peak appears, therefore, due to post-pulse irradiation, as clearly observed in figure 5(b), despite the fact that the estimated post-pulse intensity is $\sim 10^{-3}$ times lower than the main-NIR pulse. The strong REAR peak appears because a large number of Rydberg atoms are produced by

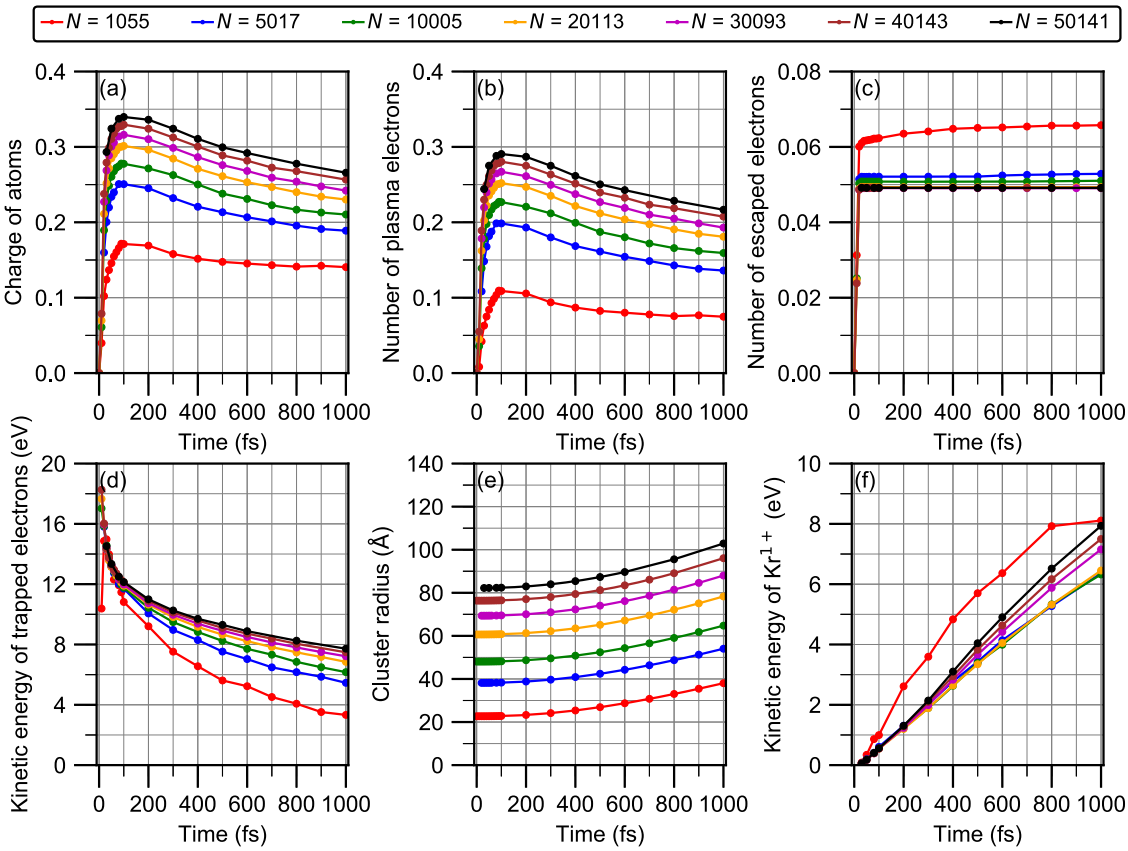

Figure 6. Time evolution of krypton clusters during the first picosecond after XFEL irradiation, obtained from simulations: (a) average charge of atoms, (b) average number of plasma electrons per atom, (c) average number of escaped electrons per atom, (d) mean kinetic energy of trapped (nanoplasma) electrons, (e) time evolution of the mean cluster radius, defined as $R = 5/3\sqrt{\frac{1}{N}\sum_{i=1}^{N} r_i^2}$, N and r being the number of atoms and the distance of an atom from the center, respectively; (f) average kinetic energy of Kr^{1+} ions. Note that panels (a) and (f) show processed data where the raw ion charges extracted from the simulation snapshots are updated according to the number of classically recombined electrons (classical recombination results in the reduction of the raw charge of some ions). Similarly, the data of panels (b) and (d) are based on electrons that are trapped in the cluster and that are still delocalized among the atoms (i.e. they are not yet recombined).

efficient electron–ion recombination during the nanoplasma expansion. According to figure 5(a), for intermediate time delays between ∼50–170 ps, electron–ion recombination is still ongoing during nanoplasma expansion.

The Rydberg atoms are already well isolated from other fragments at longer time delays (∼12.5 ns), when the photoelectrons can freely fly away without significant impact from the interaction with neighboring ions and the cluster potential. The binding energy of the Rydberg electrons is estimated to be ∼0.9 eV by subtracting the kinetic energy of the REAR peak, 0.65 eV, from the NIR photon energy, 1.55 eV. The binding energy indicates that the most probable states after the nanoplasma expansion are the $4s^2 4p^5 7s$ Rydberg state and the $4s^2 4p^5 4f$ excited valence state [62]. The long lifetimes of these states (∼24 ns and ∼60 ns, respectively), calculated with the XATOM code [38, 63], explain their survival until the arrival of the post pulse.

Since the shift of the REAR peak does not change before 170 ps, the cluster has not completely disintegrated up to the longest time delay applied and the cluster environment still has an impact on the released electron. Our experiment then shows that the expansion of Kr_{50000} is relatively slow.

4.4. Cluster dynamics triggered by an XFEL pulse: numerical simulations

In order to gain deeper insight into the ionization and real space dynamics, particularly into the early dynamics of the electron plasma initiated by the XFEL pulse, we performed simulations for the 5.6 keV photon energy case with the computational tool XMDYN [37, 38]. The goal was to reveal the source of the exponential-like continuous feature below 150 eV seen in the experimental electron energy spectra. Therefore, we did not perform focal volume integration of the signals. Instead, we picked a representative photon fluence, chosen to be 7.8×10^9 photons/μm^2, corresponding to the half of the nominal peak fluence (later we will refer to this value as *representative fluence*, F_{rep}). Under this condition, approximately 2.5% of the atoms were photoionized. Beyond the experimentally relevant cluster size of ∼50 000 atoms, we did simulations for various smaller values as well (N = 1055, 5017, 10 005, 20 113, 30 093, 40 143 and 50 141) to study the cluster-size dependence (we generated the initial cluster configurations by applying simulated annealing on a large van der Waals cluster, then cut out a spherical volume from the center so that the

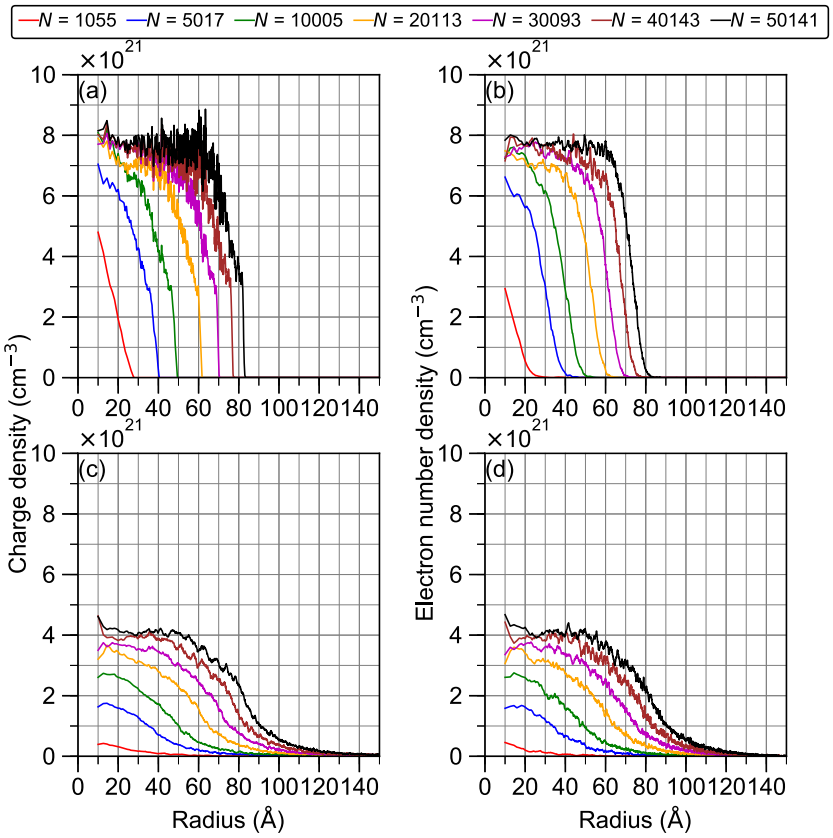

Figure 7. Average charge density and average number density of the nanoplasma electrons at early time ($t = 30$ fs) and at the end of the simulation ($t = 1$ ps) for different cluster sizes: (a) average charge density of ions at $t = 30$ fs; (b) average number density of the nanoplasma electrons at $t = 30$ fs; (c) average charge density of ions at $t = 1$ ps; (d) average number density of the nanoplasma electrons at $t = 1$ ps.

number of atoms contained was as close as possible to the nominal experimental cluster sizes). We followed the systems up to 1 ps after the center of the XFEL pulse. For each case we ran eight trajectories with different random seeds, in order to improve the statistics of the results.

Figure 6 summarizes several time-dependent cluster properties. According to figure 6(a), the average charge of the atoms first rapidly grows during irradiation. Then, for all cluster sizes, it stops increasing at ∼100 fs, after the collisional ionization cascades end. Even for the largest clusters, only one third of the atoms are ionized on average. After reaching the maximum, a gradual decrease of the average atomic charge starts. Figure 6(b) shows a very similar evolution for the number of plasma electrons. The slope of the decreasing part agrees with that of the average atomic charge curve, as both are due to the ongoing recombination. Except for the smallest investigated cluster size, practically no electrons escape at times from a few tens of femtoseconds up to 1 picosecond after the XFEL pulse (figure 6(c)). Further, the number of escaped electrons is 5.0% of the number of atoms, with contributions from the escaped *fast* photoelectrons (2.5%) and LMM Auger electrons (∼2.5%). Note that a 2p vacancy mainly yields a *fast* LMM Auger electron (with a branching ratio of ∼90% [57]), while a 2s vacancy mostly undergoes an LLM Coster–Kronig decay (with a branching ratio of ∼76% [57], releasing a *slow* electron), subsequently followed by another LMM Auger decay (releasing a *fast* electron). This justifies the scheme used in the previous section to estimate the ionization level.

A comparison between figures 6(b) and (c) shows that for the largest clusters considered, the number of electrons that manage to escape is smaller by almost an order of magnitude than the maximum number of plasma electrons. Furthermore, no plasma electrons escape from the cluster environment after the XFEL pulse is over, as seen in figure 6(c).

Figure 6(d) shows the mean kinetic energy of electrons trapped within the nanoplasma. The mean kinetic energy of trapped electrons immediately decreases after the nanoplasma formation, while the electron number still increases up to ∼100 fs. This indicates that the energetic trapped electrons lose their energy within femtoseconds via collisional ionization of neutral atoms. Therefore, throughout almost the whole evolution the plasma is cooling, first because of electrons participating in collisional ionization events and then because of recombination and expansion. The expansion is rather slow, according to figure 6(e), which shows the radius of the cluster as a function of time.

Finally, we show in figure 6(f) the average kinetic energy of the Kr^{1+} ions. The energies are comparable to the experimentally detected ones. However, clearly, the final energy has not been reached within the simulated time period (except for the smallest cluster size), hindering more detailed comparison to the experimental spectra. In the case of a 1000-atom cluster the maximal average kinetic energy of ions was reached already

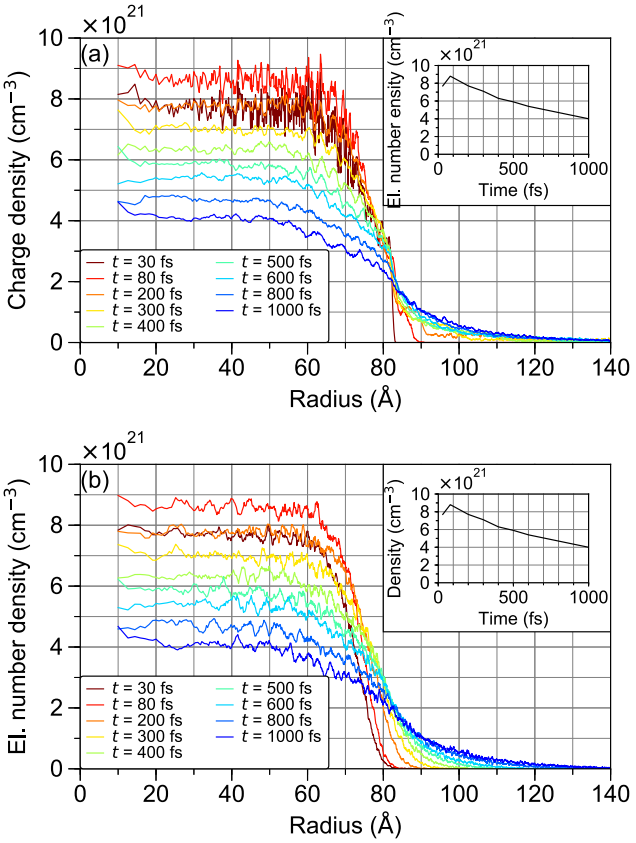

Figure 8. Average charge density and average number density of the nanoplasma electrons at different times for Kr_{50141}: (a) average charge density of ions; (b) average number density of nanoplasma electrons. Insets show the average densities of nanoplasma core as a function of time.

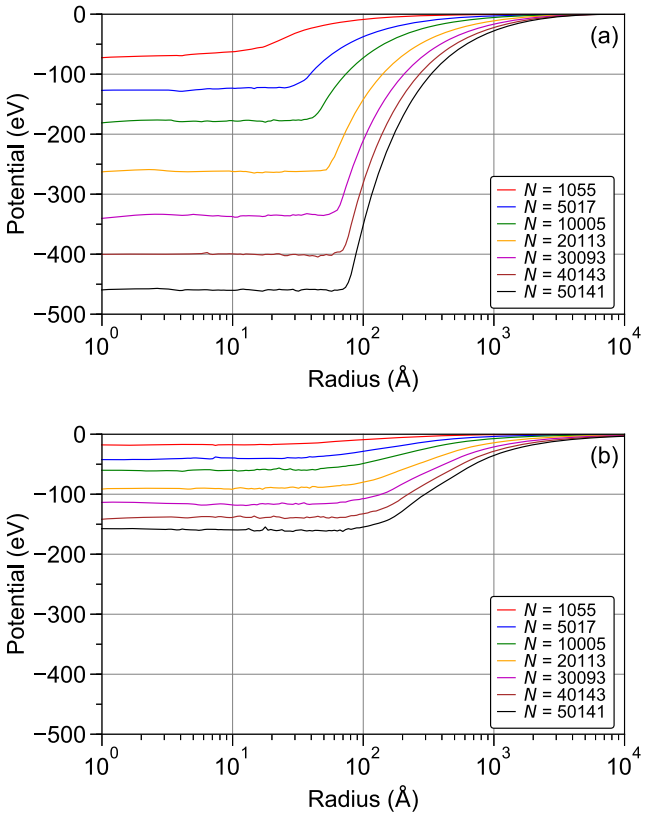

Figure 9. Trapping cluster potential for different cluster sizes: (a) trapping cluster potential at $t = 30$ fs; (b) trapping cluster potential at $t = 1$ ps.

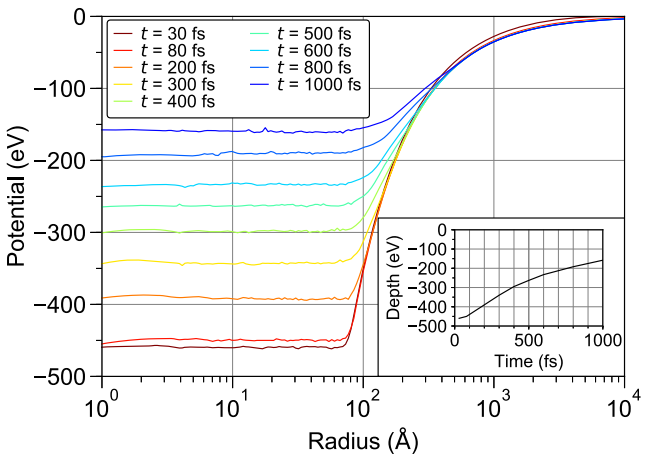

Figure 10. Trapping cluster potential at different times for Kr_{50141}. Inset shows the potential depth as a function of time.

within 1 ps after irradiation, indicating cluster disintegration. For larger clusters, similar behavior could be expected, but on much longer timescales.

In figure 7 we show the ion and electron density profiles right after the pulse is over and at the end of the simulation. Under the applied irradiation conditions, a homogeneous plasma core develops very early for sizes of 10 005 atoms and above. By $t = 1$ ps the density significantly drops due to expansion and recombination. In figure 8 we also show the density profiles at intermediate times for the largest cluster size. In the simulation, the delay at which the electron density reaches $3n_{\mathrm{crit}} = 5.1 \times 10^{21}$ cm^{-3}, fulfilling the plasma resonance condition, is ∼680 fs, with the broadening of 76 fs (out of which 44 fs can be attributed to the standard deviation emerging from the stochastic nature of the dynamics and 32 fs to statistical error). Given the experimental uncertainties, this is consistent with the experimentally found 1 ps. This confirms the interpretation of the delay-dependent Kr ion enhancement timescale regarding the role of the surface plasmon resonance.

Figure 9 shows the trapping potential for all investigated cluster sizes at $t = 30$ fs and 1 ps. While *fast* electrons leave the cluster at early times, a deep trapping potential develops that captures other quasi-free electrons (see figure 9(a)). For the largest clusters, the potential well is ∼20 times deeper than the mean kinetic energy of the nanoplasma electrons (see figure 6(d)), thus strongly reducing the probability of thermal electron evaporation. For the sake of completeness we also show the trapping potential at intermediate times for Kr_{50141} clusters in figure 10.

Based on the presented results, we conclude that the general scheme of the cluster dynamics explained above is valid

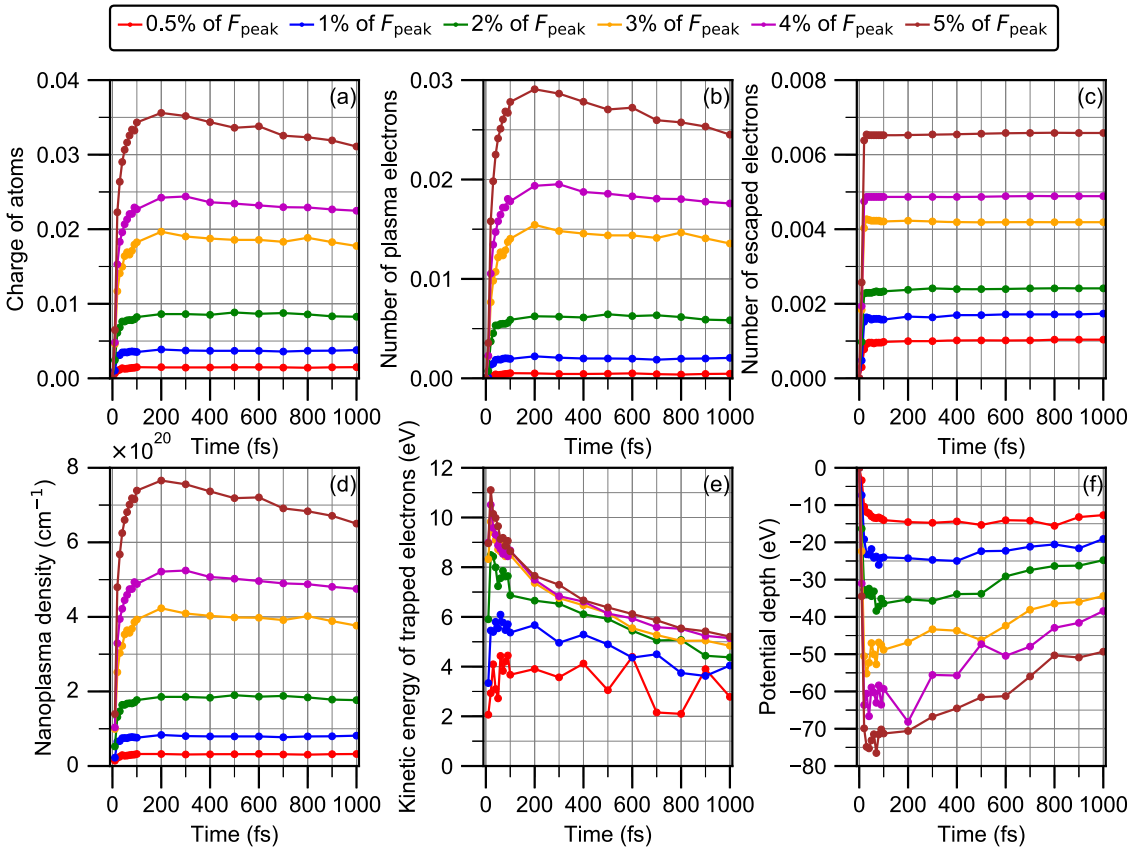

Figure 11. Time evolution of 50 141-atom krypton clusters during the first picosecond after XFEL irradiation, obtained from simulations at lower fluences: (a) average charge of atoms, (b) average number of plasma electrons per atom, (c) average number of escaped electrons per atom, (d) maximum density of nanoplasma electrons, (e) mean kinetic energy of trapped (nanoplasma) electrons, (f) cluster potential depth.

over a wide range of cluster sizes at the representative fluence F_{rep}. Although we are not aiming for an accurate simulation of the volume-integrated experimental signals, in the following we give insight into how the 50 141-atom clusters behave at lower fluences present in the halo of the focused x-ray beam. In particular, we are interested in the dynamics when a much shallower cluster potential is built up due to lower ionization level and, therefore, one may expect thermal electron evaporation even within the simulated 1 ps time period. We analyze clusters at 0.5%, 1%, 2%, 3%, 4% and 5% of the nominal peak fluence F_{peak} (these values are 1%, 2%, 4%, 6%, 8% and 10% of the representative fluence F_{rep}, respectively). For this demonstration, we use one trajectory per fluence value. Figures 11(a)–(f) show the properties of the system as a function of time for the selected fluence values. The average charge of atoms, the average number of plasma and escaped electrons, and the maximum nanoplasma density of the nanoplasma electrons show a roughly linear dependence on the applied x-ray fluence. While the nanoplasma density does not reach the NIR resonance critical density ($3n_{crit} = 5.1 \times 10^{21}$ cm^{-3}) in any of the simulated low-fluence cases (figure 11(d)), we can estimate (using the approximate linear dependence on the fluence) that the critical fluence to generate a sufficiently dense plasma for the resonance response is around 30% of the nominal peak fluence F_{peak} (equal to 60% of F_{rep}). This means that NIR-resonance-caused delay-dependent features in the pump–probe signals are built up due to the response of clusters in the high fluence region of the x-ray beam. The mean kinetic energy of the plasma electrons is a few eV throughout the simulated 1 ps interval (figure 11(e)). It gradually decreases. However, the speed of cooling significantly drops when lowering the fluence. Even in the case of low fluences (0.5% of F_{peak}), one finds the trapping potential deep enough (∼10 eV) to hinder any thermal emission before ∼1 ps (figure 11(e)).

We end this section by discussing the possible consequences of omitting some of the electron-correlation-driven decay phenomena in the model, e.g. ETMD and the processes connecting classically treated and *quantum-modeled* electrons and states. In a system of ground-state Kr^{1+} ions and classical electrons our modeling framework would include correlated phenomena (on the classical level, of course). However, e.g. in a simulated 50 141-atom cluster (exposed to F_{rep}), at 1 ps there are also approximately 700 excited states Kr^{1+} and 2800 highly charged ion cores (with charge 2 and above) present (we note that most of them have undergone classical recombination). We use the energy released, if these ions became ground-state neutral atoms, as a conservative estimate for the upper limit of the energy that could be transferred to the plasma electron subsystem via the disregarded correlated processes. This estimation yields ∼7 eV/atom, which would be enough to generate, on average, an additional 7 eV/(13 eV + 8 eV) ∼ 0.3 classical plasma electrons per atom at 8 eV

average kinetic energy (13 eV being the ionization energy of krypton). While this is a significant amount, indicating the general importance of the missing correlated processes in the modeling framework, including them would not qualitatively change the picture of the dynamics. Finally, we note that the possible underestimation of the plasma electron density can lead to an earlier occurrence of the NIR resonance in our simulation, describing the discrepancy observed in the comparison between simulation and experiment.

4.5. Highly suppressed thermal emission of nanoplasma electrons

Electron spectra observed in the experiments on transient nanoplasma typically contain a feature that can be directly connected to the thermal condition of the trapped electrons. Moreover, this feature reflects the conditions in clusters excited in the focus of an applied laser pulse, i.e. where the largest energy absorption inside a cluster occurs [18]. This feature manifests as an exponential-like drop in the kinetic energy spectrum from zero toward higher energies, representing thermal electron emission. In this section we show that none of the features of the electron spectra in our experiment can be connected to thermal emission of nanoplasma generated in the XFEL beam focus.

First, we investigate the exponentially decaying feature in the energy region between ∼20 and 120 eV (figure 12(b)). This feature can be fitted using an exponential with a characteristic energy in the range of 50–100 eV, depending on the cluster size. The available plasma temperatures are expected to be below ∼10 eV because of the rapid cooling of electrons trapped within the nanoplasma (see figure 6(d)). The extracted decay constants (50–100 eV, also consistent with the experimental value of 62 eV) are much higher than the available plasma temperatures. Our analysis of individual electron trajectories shows that the majority (∼80%) of the electrons below ∼120 eV are produced via collisional ionization by *fast* (photo- or LMM Auger) electrons, with ∼12% being *slow* LLN, MMN or MNN Auger electrons, escaping at a very early stage without losing energy through collisional ionization. Finally, the remaining ∼8% are originally *fast* LMM Auger electrons that have lost most of their energy in a sequence of collision ionization events. Therefore, we can conclude that, according to the simulations, the electrons contributing to this part of the spectra escape from the cluster directly after being emitted from an atom. The same conclusion is valid for the signal coming from clusters located in low-x-ray-fluence regions (see the electron kinetic energies in figure 11(e)).

Now we analyze the 1–20 eV energy range in the spectrum, to which correlated decay phenomena (yielding emission of $\lesssim$20 eV electrons) and late plasma emission (at a stage when the trapping potential is shallow enough) could contribute. We argue that no visible contribution of plasma emission can originate from the high-fluence region in the focused beam. Here, we define the high-fluence region of the focus as a region where the ionization of a cluster is high enough to create plasma electron densities reaching the critical NIR resonance value (according to section 4.4, this is at least 30% of the nominal peak fluence). Below 1 ps, i.e. before the resonance

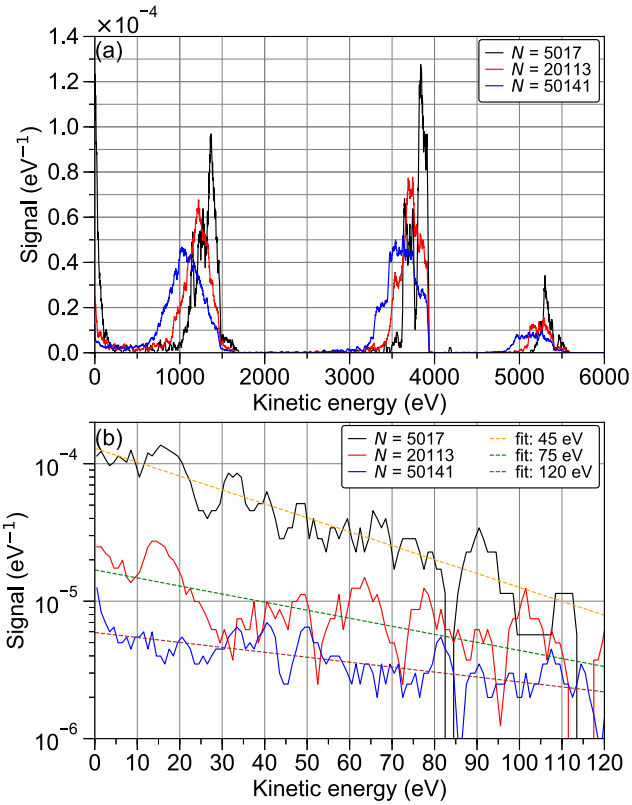

Figure 12. Simulated KES of the escaping electrons at $t = +1$ ps for three different cluster sizes. The curves correspond to the number of electrons within a 1 eV energy bin divided by the number of cluster atoms N. (a) Larger cluster size results in broader peaks of the escaping Auger and photoelectrons (around 1.5 keV and around 4 keV and 5.5 keV, respectively) and in a suppressed number of electrons below ∼100 eV. (b) Spectra exhibit an exponential decay below 120 eV. However, electrons escaping at very early times, directly after their release at ionization and without significant energy transfer with other plasma electrons, also contribute to this part of the spectra. Therefore, it cannot be attributed to thermal emission of nanoplasma electrons. Note that the peak feature in (b) below 5 eV for $N = 50\,141$ is an artifact of the 5 eV broad smoothing applied on the data.

condition is reached during the dynamics, the simulations show that the deep cluster potential hinders thermal emission. At resonance, which happens at around 1 ps, the ion kinetic energies are enhanced remarkably (figure 3). This indicates that a significant amount of energy is absorbed from the NIR pulse. As energy absorption happens via the electron plasma subsystem, it is reasonable to expect any delay-dependent signature in a thermal emission signal. However, our detected electron spectra show no delay dependence whatsoever, neither of the slope (i.e. nanoplasma temperature) nor of the signal strength (i.e. the number of emitted electrons). Regarding the emission due to correlated decay phenomena at early times, similar reasoning can be used. While these processes definitely occur during cluster expansion, locally ejected electrons cannot leave the cluster for several picoseconds, i.e. while the trapping potential is deep. However, at a late stage of expansion, when the trapping potential drops, electrons may be released via these processes, also adding irregularities to the KES (figure 2(b)). Finally, we highlight that the electrons

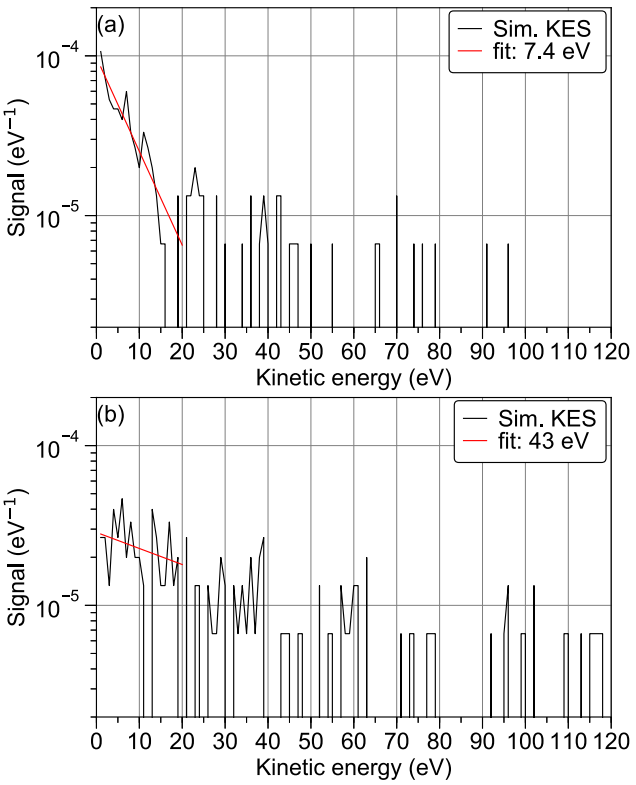

Figure 13. Simulated KES of electrons escaping from 50 141-atom clusters at $t = +1$ ps for lower fluences. (a) Average of 0.5%, 1% and 2% of F_{peak} cases; (b) average of 3%, 4% and 5% of F_{peak} cases.

coming from very low-fluence regions may also contribute to the 1–20 eV kinetic energy range. This is already suggested by the observation of prompt electron emission occurring at early times in the simulations (figure 13). However, a contribution from later-stage thermal emission and correlated decay phenomena cannot be ruled out either.

To sum up, the absence of observable thermal emission is a consequence of the following facts: (i) A significant number of high-energy electrons can escape promptly after x-ray excitation. When ionizing with hard x-rays, this is always the case. When the photon energy is much higher than the core-electron binding energy in light elements, photoelectrons are energetic. In heavy elements, Auger electrons associated with the relaxation of deep core holes are typically also *fast* enough to escape. Under such circumstances, a strong cluster potential can form, with a depth of many hundreds of electronvolts. (ii) The nanoplasma temperature developed due to the irradiation stays well below the depth of the trapping potential. In the systems studied here, the cluster remains partially ionized, i.e. the average atomic charge remains below 1, even after collisional ionization. This ensures low kinetic temperatures (below 20 eV), as more energetic trapped electrons lose their surplus energy in collisional ionization events. The kinetic temperature increases further, once all neutral atoms become ionized. After this, the achievable maximum temperature is controlled by the ionization energy of the singly charged ions.

5. Conclusion

In order to study the nanoplasma formation in the hard x-ray regime, we conducted ion and electron spectroscopy study of krypton clusters with an average size of ∼50 000 atoms, after irradiating them with XFEL pulses with photon energies of 5.6 and 14.5 keV. The observed oligomer yield distributions show trends that are similar to those observed in earlier studies on argon clusters. The kinetic energy distributions of the ionic oligomer fragments emitted during the nanoplasma expansion are similar (up to a scaling factor) for both x-ray photon energies. This scaling property can be attributed to the scaling properties of the Coulomb explosion and hydrodynamical expansion, driving the disintegration of the clusters. When applying the XFEL pump–NIR probe technique to investigate the time evolution, the ion yield enhancement shows an expected delay dependence, with a maximum at 1 ps delay. The enhancement is attributed to enhanced energy absorption from the NIR field when the nanoplasma electron density reaches a critical value defined by the condition for surface plasmon resonance. However, the electron KES show no delay dependence, except for the enhancement seen at very low (<50 meV) energies. To obtain more detailed insight into the dynamics, we performed numerical simulations of XFEL-ionized clusters. The calculations show that over the whole simulated 1 ps time period, the plasma electrons remain strongly trapped in the deep cluster potential. However, some of the electrons escaping directly during the XFEL pulse without participation in the plasma thermalization give rise to an exponential high-energy feature in the observed kinetic energy spectrum. Features connected to the ionization of Rydberg atoms formed during recombination in the expanding system can also be identified. As the thermal emission of plasma electrons from the heavily ionized clusters is highly suppressed, the recombination features together with prompt electron emission signal and possible traces of correlated decay phenomena are the only signatures of the transient nanoplasma in the electron spectra. The simulations show that this behavior is present over a wide range of cluster sizes and can be expected upon irradiation using intense hard-x-ray pulses.

Author contributions

YK, WX, HF, KN and KU conceived the experiment. KU coordinated the experimental team. YK, WX, HF, KM, DY, KN, SW, YI, TsT, SY, TN, TU, MP, TB and MM set up the experiment. SO and TaT prepared the femtosecond optical laser pulses. YK, WX, HF, KM, DY, KN, SW, YI, TsT, SY, YS, TN, TU, MP, JDB, CM, TB, MM, EK and KU conducted the experiment. YK, WX, KM and DY analyzed the data. ZJ, VS, S-KS, BZ, and RS provided theoretical calculations. YK, ZJ, BZ, RS and KU interpreted the data and wrote the paper.

Funding

This study was supported by the X-ray Free Electron Laser Utilization Research Project and the X-ray Free Electron Laser Priority Strategy Program of the Ministry of Education, Culture, Sports, Science and Technology of Japan (MEXT), by the Proposal Program of SACLA Experimental Instruments of RIKEN, by the Japan Society for the Promotion of Science (JSPS) KAKENHI Grants Nos. JP21244042, JP23241033, JP15K17487, JP16K05016, and JP19H04392 by MEXT KAKENHI Grant No. JP22740264, by the IMRAM project, and by the National Nature Science Foundation of China Grant No. 11604003. HF and KU acknowledge support by the Dynamic Alliance for Open Innovation Bridging Human, Environment and Materials. DI and YI acknowledge support by IMRAM, Tohoku University. TsT acknowledges support by JSPS KAKENHI Grant No. JP16J02270. KN and SW acknowledge support by the Research Program of 'Dynamic Alliance for Open Innovation Bridging Human, Environment and Materials' in 'Network Joint Research Center for Materials and Devices.' TN acknowledges support by the Research Program for Next Generation Young Scientists of 'Dynamic Alliance for Open Innovation Bridging Human, Environment and Materials' in 'Network Joint Research Center for Materials and Devices.'

Acknowledgments

We are grateful to the late Makoto Yao for his invaluable contributions to the present work. The experiments were performed at SACLA with the approval of JASRI and the program review committee (No. 2014B8057).

Data availability statement

The data that support the findings of this study are available upon reasonable request from the authors.

ORCID iDs

Yoshiaki Kumagai https://orcid.org/0000-0002-2492-4676
Hironobu Fukuzawa https://orcid.org/0000-0002-8283-381X
Kiyonobu Nagaya https://orcid.org/0000-0001-9867-0800
Shin-ichi Wada https://orcid.org/0000-0002-6417-3248
Toshiyuki Nishiyama Hiraki https://orcid.org/0000-0001-6712-6335
Minna Patanen https://orcid.org/0000-0002-2970-7494
John D Bozek https://orcid.org/0000-0001-7486-7238
Ioan Dancus https://orcid.org/0000-0002-8628-3819
Catalin Miron https://orcid.org/0000-0002-8302-7158
Shigeki Owada https://orcid.org/0000-0002-1451-7612
Sang-Kil Son https://orcid.org/0000-0001-5395-632X
Beata Ziaja https://orcid.org/0000-0003-0172-0731
Robin Santra https://orcid.org/0000-0002-1442-9815

References

[1] Ackermann W *et al* 2007 *Nat. Photon.* **1** 336–42
[2] Emma P *et al* 2010 *Nat. Photon.* **4** 641–7
[3] Ishikawa T *et al* 2012 *Nat. Photon.* **6** 540–4
[4] Young L *et al* 2010 *Nature* **466** 56–61
[5] Vinko S M *et al* 2012 *Nature* **482** 59–62
[6] Yoneda H *et al* 2015 *Nature* **524** 446–9
[7] Mankowsky R *et al* 2014 *Nature* **516** 71–3
[8] Kim K H *et al* 2015 *Nature* **518** 385–9
[9] Wernet P *et al* 2015 *Nature* **520** 78–81
[10] Chapman H N *et al* 2011 *Nature* **470** 73–7
[11] Seibert M M *et al* 2011 *Nature* **470** 78–81
[12] Redecke L *et al* 2013 *Science* **339** 227–30
[13] Kang H S *et al* 2017 *Nat. Photon.* **11** 708–13
[14] Decking W *et al* 2020 *Nat. Photon.* **14** 391–7
[15] Milne C J *et al* 2017 *Appl. Sci.* **7** 720
[16] Seddon E A *et al* 2017 *Rep. Prog. Phys.* **80** 115901
[17] Young L *et al* 2018 *J. Phys. B: At. Mol. Opt. Phys.* **51** 032003
[18] Saalmann U, Siedschlag C and Rost J M 2006 *J. Phys. B: At. Mol. Opt. Phys.* **39** R39
[19] Fennel T, Meiwes-Broer K-H, Tiggesbäumker J, Reinhard P-G, Dinh P M and Suraud E 2010 *Rev. Mod. Phys.* **82** 1793–842
[20] Thomas H *et al* 2012 *Phys. Rev. Lett.* **108** 133401
[21] Gorkhover T *et al* 2012 *Phys. Rev. Lett.* **108** 245005
[22] Tachibana T *et al* 2015 *Sci. Rep.* **5** 10977
[23] Bostedt C *et al* 2008 *Phys. Rev. Lett.* **100** 133401
[24] Arbeiter M and Fennel T 2010 *Phys. Rev.* A **82** 013201
[25] Thomas H *et al* 2009 *J. Phys. B: At. Mol. Opt. Phys.* **42** 134018
[26] Arbeiter M and Fennel T 2011 *New J. Phys.* **13** 053022
[27] Last I and Jortner J 2000 *Phys. Rev.* A **62** 013201
[28] Rusek M and Orłowski A 2005 *Phys. Rev.* A **71** 043202
[29] Ziaja B, Wabnitz H, Weckert E and Möller T 2008 *New J. Phys.* **10** 043003
[30] Hoener M *et al* 2008 *J. Phys. B: At. Mol. Opt. Phys.* **41** 181001
[31] Schütte B, Arbeiter M, Fennel T, Vrakking M J J and Rouzée A 2014 *Phys. Rev. Lett.* **112** 073003
[32] Schütte B, Campi F, Arbeiter M, Fennel T, Vrakking M J J and Rouzée A 2014 *Phys. Rev. Lett.* **112** 253401
[33] Schütte B, Oelze T, Krikunova M, Arbeiter M, Fennel T, Vrakking M J J and Rouzée A 2015 *New J. Phys.* **17** 033043
[34] Gnodtke C, Saalmann U and Rost J M 2009 *Phys. Rev.* A **79** 041201
[35] Kumagai Y *et al* 2020 *Phys. Rev.* A **101** 023412
[36] Kumagai Y *et al* 2018 *Phys. Rev. Lett.* **120** 223201
[37] Murphy B F *et al* 2014 *Nat. Commun.* **5** 4281
[38] Jurek Z, Son S-K, Ziaja B and Santra R 2016 *J. Appl. Crystallogr.* **49** 1048–56
[39] Inubushi Y *et al* 2012 *Phys. Rev. Lett.* **109** 144801
[40] Yabashi M *et al* 2013 *J. Phys. B: At. Mol. Opt. Phys.* **46** 164001
[41] Yumoto H *et al* 2013 *Nat. Photon.* **7** 43–7
[42] Tono K, Kudo T, Yabashi M, Tachibana T, Feng Y, Fritz D, Hastings J and Ishikawa T 2011 *Rev. Sci. Instrum.* **82** 023108
[43] Fukuzawa H *et al* 2013 *Phys. Rev. Lett.* **110** 173005
[44] Motomura K *et al* 2013 *J. Phys. B: At. Mol. Opt. Phys.* **46** 164024
[45] Hagena O F 1981 *Surf. Sci.* **106** 101–16
[46] Katayama T *et al* 2016 *Struct. Dyn.* **3** 034301
[47] Kumagai Y *et al* 2018 *Phys. Rev.* X **8** 031034
[48] Fukuzawa H, Nagaya K and Ueda K 2018 *Nucl. Instrum. Methods Phys. Res.* A **907** 116–31
[49] Cederbaum L S, Zobeley J and Tarantelli F 1997 *Phys. Rev. Lett.* **79** 4778–81
[50] Zobeley J, Santra R and Cederbaum L S 2001 *J. Chem. Phys.* **115** 5076–88
[51] Kuleff A I, Gokhberg K, Kopelke S and Cederbaum L S 2010 *Phys. Rev. Lett.* **105** 043004

[52] Schütte B, Arbeiter M, Fennel T, Jabbari G, Kuleff A I, Vrakking M J J and Rouzée A 2015 *Nat. Commun.* **6** 8596
[53] Schütte B *et al* 2018 *Phys. Rev. Lett.* **121** 063202
[54] Henke B L, Gullikson E M and Davis J C 1993 *At. Data Nucl. Data Tables* **54** 181–342
[55] Lotz W 1967 *Z. Phys.* **206** 205–11
[56] Krause M O and Carlson T A 1967 *Phys. Rev.* **158** 18–24
[57] Kochur A G, Dudenko A I, Sukhorukov V L and Petrov I D 1994 *J. Phys. B: At. Mol. Opt. Phys.* **27** 1709
[58] Toyota K *et al* 2019 *J. Synchrotron Radiat.* **26** 1017–30
[59] Gitomer S J, Jones R D, Begay F, Ehler A W, Kephart J F and Kristal R 1986 *Phys. Fluids* **29** 2679–88
[60] Ditmire T, Donnelly T, Rubenchik A M, Falcone R W and Perry M D 1996 *Phys. Rev.* A **53** 3379–402
[61] Kelbg M, Heidenreich A, Kazak L, Zabel M, Krebs B, Meiwes-Broer K-H and Tiggesbäumker J 2018 *J. Phys. Chem.* A **122** 8107–13
[62] Saloman E B 2007 *J. Phys. Chem. Ref. Data* **36** 215–386
[63] Son S-K, Young L and Santra R 2011 *Phys. Rev.* A **83** 033402